Spatial Heterogeneity of Uplift Pattern in the Western European Alps Revealed by InSAR Time Series Analysis

Marguerite Mathey[1,1], Marie-Pierre Doin[2,2], Pauline André[3,3], Andrea Walpersdorf[4,4], Stéphane Baize[5,5], and Christian Sue[1,1]

[1]Université Grenoble Alpes
[2]Institut des Sciences de la Terre
[3]Université Grenobles Alpes
[4]ISTERRE
[5]IRSN

November 30, 2022

Abstract

The Western European Alps display measurable surface deformation rates from levelling and GNSS data. Based on the time-series analysis of 4 years of Sentinel-1 data, we propose for the first time an InSAR-based mapping of the uplift pattern affecting the Western Alps on a ˜350x175- km-wide area. This approach provides a denser spatial distribution of vertical motion despite the high noise level inherent to mountainous areas and the low expected deformation signal. Our results show consistency with other geodetic measurements at the regional scale, and reveal smaller-scale spatial variations in the uplift pattern. Higher uplift rates are found within the external crystalline massifs compared to surrounding areas, in agreement with the variations expected from recent deglaciation and long-term exhumation data. This work brings the first InSAR-based geodetic clue of differential uplift within the Alpine belt in response to the surface and deep processes affecting the belt.

Spatial Heterogeneity of Uplift Pattern in the Western European Alps Revealed by InSAR Time-Series Analysis

M. Mathey[1], M.-P. Doin[1], P. André[1], A. Walpersdorf[1], S. Baize[2], C. Sue[1,3]

[1]University Grenoble Alpes, University Savoie Mont Blanc, CNRS, IRD, IFSTTAR, ISTerre, Grenoble, 38000, France.

[2]IRSN,PSE-ENV/SCAN/BERSSIN, BP 17, Fontenay-aux-roses, F-92262, France.

[3]Chrono-Environnement Besançon, OSU THETA, University Bourgogne-Franche-Comté, Besançon, 25000, France.

Corresponding author: Marguerite Mathey (marguerite.mathey@univ-grenoble-alpes.fr)

Key Points:

- We use four years of Sentinel-1 radar acquisitions to derive interseismic line-of-sight velocities over the Western European Alps.
- InSAR-derived velocities are consistent with other geodetic studies and provide increased spatial resolution of surface velocity patterns.
- Short-wavelength spatial variations show locally higher velocities localized on crystalline massifs, interpreted as higher uplift rates.

Abstract

The Western European Alps display measurable surface deformation rates from levelling and GNSS data. Based on the time-series analysis of 4 years of Sentinel-1 data, we propose for the first time an InSAR-based mapping of the uplift pattern affecting the Western Alps on a ~350x175-km-wide area. This approach provides a denser spatial distribution of vertical motion despite the high noise level inherent to mountainous areas and the low expected deformation signal. Our results show consistency with other geodetic measurements at the regional scale, and reveal smaller-scale spatial variations in the uplift pattern. Higher uplift rates are found within the external crystalline massifs compared to surrounding areas, in agreement with the variations expected from recent deglaciation and long-term exhumation data. This work brings the first InSAR-based geodetic clue of differential uplift within the Alpine belt in response to the surface and deep processes affecting the belt.

Plain Language Summary

The surface of the Earth is constantly moving from about a few millimeters to a few centimeters per year in response to geological processes such as tectonic plate motions and gravitational re-equilibrium. In the Western European Alps, where the mountain-building phase of the belt is over, the processes at the origin of surface motions are under debate. Mapping surface displacements at the highest possible resolution is mandatory to better understand the evolution of the Alpine belt. Among other techniques, radar satellites can provide measurements of such displacements. Here, radar images from the recent Sentinel-1 satellite allow us to improve the spatial resolution of vertical surface displacements in the Western Alps compared to previous techniques. Thanks to the unmatched frequency of acquisitions from this satellite, we are able for the first time in our study area to measure small-scale spatial variations within the vertical motions. These variations appear correlated to distinct geological units. This brings new insights into the geological processes acting nowadays on the Western Alps.

1 Introduction

The European Alpine belt results from the complex continental collision phases between Africa and Eurasia (Schmid and Kissling, 2000; Coward and Dietrich, 1989). While convergence is still active and is attested by Adria indentation in the Eastern and Central Alps, it stopped in the

Western Alps, where the present-day kinematics are characterized by the anticlockwise rotation of Adria microplate with respect to Eurasia (e.g. Calais et al., 2002). Global Navigation Satellite System (GNSS) measurements highlight extensive and transcurrent horizontal strain rates in the western part of the belt, without any measured shortening across it (Calais et al., 2002; Serpelloni et al., 2016; 2018). The dynamic processes that have been suggested to affect the Western Alps involve intrinsic surficial (isostatic adjustments to deglaciation and erosion) and deep sources (slab pull or break-off and mantle upwelling), as well as far-field microplate kinematics, but their respective contributions to present-day crustal deformation are an ongoing debate (e.g. Sternai et al., 2019).

GNSS and levelling measurements in the Western Alps indicate that vertical velocities of a few mm/yr are expected, which is an order of magnitude higher than the horizontal motions (Masson et al., 2019; Nocquet et al., 2016; Walpersdorf et al., 2018; Mathey et al., 2020). Increasing the spatial resolution of vertical motions is thus of primary importance to understand the processes at the origin of surface deformation within the belt. Despite the dense coverage of GNSS networks over the Alps, the velocity fields obtained after spatial interpolation of GNSS velocity data strongly depend on the method, and can be highly impacted by the inclusion of one or a few outlier velocities. Interferometric Synthetic Aperture Radar (InSAR) imagery constitutes a complement to GNSS measurements to assess the spatial extent of regional deformation since it provides continuous estimates of surface displacements and a high sensitivity to the vertical component. InSAR data have not been used, up to now, to map slow, large-scale deformation across the European Alps, but only for landslide monitoring (e.g. Aslan et al., 2020; Singh et al., 2005), because of (1) the low expected long-term surface deformation signal compared to the atmospheric noise induced by high topographic gradients within the belt, and of (2) the temporal decorrelation related to vegetation and snow coverage changes over seasons. While several similar works already focused on mountainous areas worldwide (e.g. Daout et al., 2019; Grandin et al., 2012; Hammond et al., 2012), they were all focusing on areas with higher signal-to-noise ratios.

The launching of the Sentinel-1 radar satellite in 2014 now enables us to derive InSAR estimates of tectonic surface velocities for the first time across the Western Alps. Here we assess the spatial extent of the regional vertical signal based on the time-series analysis of more than 700 interferograms computed over 4 years of radar acquisitions.

2 Sentinel-1 data processing

We use Sentinel-1 acquisitions along ascending track A088 ranging from November 2014 to December 2018. Sentinel-1 interferometric wide-swath mode acquires data on a swath width of about 250 km. We limited our analysis to the sub-swaths 1 and 2, covering our area of interest by 175 km in range and 350 km in azimuth (Figure 1a). To extract the ground velocity signal, data were processed using the New Small BAseline Subset (NSBAS) chain developed by Doin et al. (2011). Single Look Complex (SLC) images were all coregistered on a reference date before computing differential interferograms. Interferograms have first been multi-looked by a factor 2 in azimuth and 8 in range. Precise orbits from the Copernicus Precise Orbit Determination Service (Peter et al., 2017) and the SRTM digital elevation model (Farr et al., 2007) were used in order to correct the geometrical phase difference between acquisitions. The phase correction within each burst due to the backward-forward sweeping of the radar antenna was performed in two steps (Grandin, 2015): first, an azimuth adjustment quantified by image coregistration, and second, a multi-linear adjustment of the backward-forward interferograms obtained with the spectral diversity method in the burst-overlap areas (Scheiber & Moreira, 2000). Spectral diversity parameters are inverted into time series to avoid a drift due to cumulative noise. Then, the corresponding phase correction is directly applied on the interferograms.

The European Alps are affected by large snow cover and by vegetation changes in forests and crop lands, which both reduce the interferometric coherence. The former affects mainly winter dates whereas the latter effect has the strongest impact in spring and early summer. As we are interested in large-scale deformation patterns, we must ascertain phase continuity across the Alps, mainly relying on valleys in winter and on summits in summer, with flanks often covered by forests. Therefore, optimizing the interferogram network has the utmost importance: we performed a systematic analysis of each interferogram coherence and of all interferograms with a given acquisition. This led us to discard a few dates because of their particularly large snow cover. Furthermore, the coherence analysis per date helped us to select image pairs with the longest temporal baselines. Acquisitions from September to November were generally found the most appropriate to combine with other dates. Interferograms crossing the snow period in particular were chosen with great care. Finally, 173 dates and 734 interferograms remain (Figure 1b) with temporal baselines ranging from 6 days to one year (Figure 1c). In spite of the selection of the best

interferograms in terms of coherence, interferogram unwrapping remained challenging, and required several preceding corrections detailed hereafter.

The Atmospheric Phase Screen (APS) of interferograms due to pressure, temperature, and humidity changes in the atmosphere makes unwrapping particularly challenging in mountainous areas and limits the accuracy of InSAR measurements (Zebker et al., 1997; Hanssen, 2001; Elliott et al., 2008; Doin et al., 2009). Atmospheric changes produce both an elevation-dependent phase, called stratified atmospheric effect, and atmospheric patterns, mostly random in space and time. Steep slopes in the Alps, whose shortening in radar geometry is stronger for the radar facing flanks, produce narrow fringes. This effect, when added to the decorrelation due to forests, can lead fringes on the radar facing flanks to disappear and produce unwrapping ambiguities. To limit this effect, interferograms were corrected before unwrapping using ERA5 atmospheric model reanalysis (Hersbach et al., 2020) as described in Doin et al. (2009) and Jolivet et al. (2011). We validated this correction by comparing it to the empirical phase-versus-elevation ratio (Doin et al., 2009; 2015; Grandin et al., 2012), and found that it successfully removed the seasonal evolution of the phase-elevation relationship and reduced its day-to-day variability. However, the smooth model elevation of ERA5 (Figure 1a) displays values of 1000 to 2000 m for the points closest to deeply incised valleys (e.g. Sion and Aosta Valleys, Figure 1a). As a result, the correction applied along these valleys, which is obtained by downward extrapolation, is less precise (see section 3).

Once the interferograms were corrected from stratified atmospheric fringes, we replaced the amplitude of the interferogram by the colinearity measurement (Pinel-Puysségur et al., 2012). We then applied a second step of multilooking to 32x8 looks, in which pixels are weighted according to the colinearity, thus increasing the overall signal to noise ratio.. This process makes fringe continuity clearer in noisy areas (Daout et al., 2017). We then applied an adaptive Gaussian filter with a moving window. Phase unwrapping, performed in the spatial domain by region growing (Doin et al., 2015; Grandin et al., 2012), starts in the most coherent area and expands progressively to the lowest coherence areas. Here, we combine the coherence criterion to the topographic slope in radar geometry to prevent the phase-unwrapping path to cross the steepest slopes and those facing the radar. Remaining unwrapping errors were systematically checked for all the 734 interferograms and corrected by adjusting the erroneous number of phase cycles between patches. We then applied a “snow” mask on interferograms, based on a threshold on the

averaged coherence per date, for the two dates constituting the interferogram.

Finally, unwrapped interferograms were corrected from orbital ramp residuals by adjusting a linear phase ramp of the form:

$$ax + by + c \quad (1)$$

where x is the range and y the azimuth directions and c a constant.

The *a* and *b* parameters are then used to invert into time series a_l and b_l for each time step *l*. The phase ramp is corrected from interferograms using reconstructed parameters, as shown in Biggs et al. (2007).

Time series of cumulative surface displacements are obtained by the inversion of all interferograms (Doin et al., 2015). Inversion quality depends on the consistency of interferometric phase differences within the interferogram network (Lopez Quiroz et al., 2009). Remaining unwrapping errors can then be detected and corresponding interferogram patches are either corrected or, if not possible, masked. Finally, the Root Mean Square of the network phase misclosure (hereafter called misclosure RMS) is around 0.4 radians, indicating a high-quality unwrapping (Figure S1a). A threshold of 0.5 radians on the misclosure RMS map was used to mask the least coherent pixels. Another quality indicator lies in the average misclosure of short temporal baseline interferograms (called hereafter Misclosure of Low Duration Interferograms or MLDI), which can be either positive or negative. The corresponding maps are computed for 6, 12, or 18-days interferograms. They quantify the bias associated with seasonal vegetation growth, which is introduced by interferogram multi-looking nonlinearity, and which fades with interferogram duration (Ansari et al., 2020). Pixels with large positive or negative bias on the 18-days MLDI map were masked (Figure S1b). Since MLDI is in fact a measure of the consistency between short and long temporal baseline interferograms, it cannot be estimated for pixels where only few long temporal baseline interferograms are available. Therefore, pixels with an average temporal baseline below 0.102 year were also masked (Figure S1c).

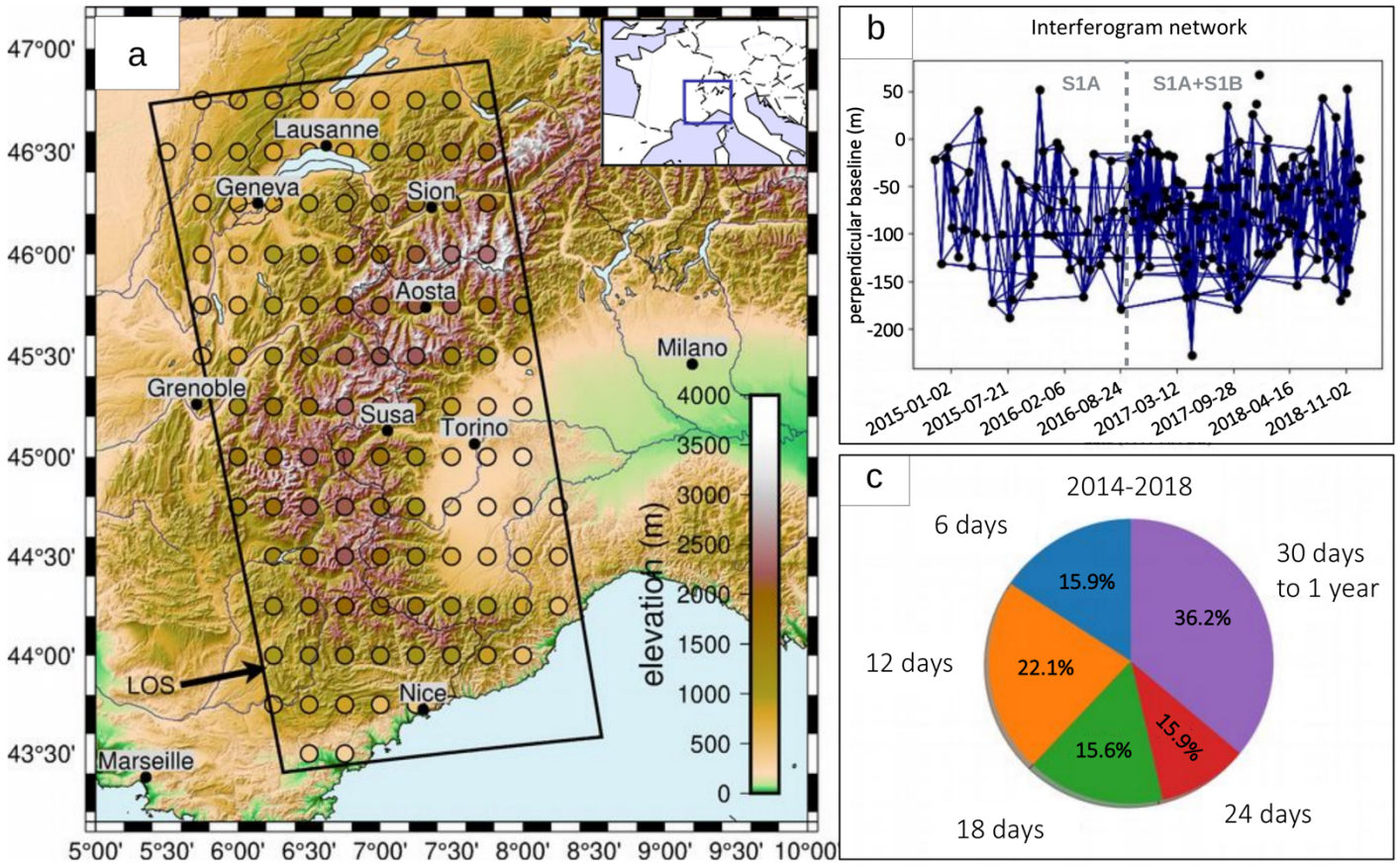

Figure 1. Study area and processed dataset. **a)** Color shaded map of the digital elevation model (Farr et al., 2007) overlaid by the Sentinel-1 footprint (track A088, black rectangle) and by circles showing ERA5 grid points color-coded according to the smooth ERA5 surface-elevation model. **b)** Processed interferogram pairs (blue lines) between radar acquisition dates (black dots) arranged by perpendicular baseline and time. The dotted line shows the starting date of Sentinel-1 B acquisitions. **c)** Proportion of interferogram durations corresponding to the interferometric network in b).

3 Ground velocity estimates from time-series inversion

A preliminary line-of-sight (LOS) velocity map was obtained by linear regression of the inverted phase-delay time series (Figure S2a). This map showed numerous local instabilities affecting valley flanks, as for example in Aosta Valley, almost systematically compatible with downward along-slope displacements. These motions compared well with the geographical extent of the numerous field-based mapped Deep-seated Gravitational Slope Deformations (DSGSD) (Agliardi et al., 2001; Drouillas et al., 2020; Hippolyte et al., 2006, Blondeau et al., 2021), and with InSAR measurements of DSGSD in the southern part of our study area (Aslan et al., 2020). Here, we used the DSGSD inventory made by André (2020) extracted as follows: (1) high-pass filtered interferograms were inverted into time series to obtain a high-pass filtered velocity map; (2) a threshold was applied on velocity; (3) additional constraints were applied on size, slope amplitude and orientation with respect to radar viewing angle, and radar visibility. Pixels affected by DSGSD or possibly by other non-tectonic localized processes were then masked on the velocity map (Figure S1d).

Although the amplitude of the residual APS is large compared to deformation, the data set contains N=173 independent acquisitions, thus reducing the uncertainty on the velocity estimate obtained by regression by $\sqrt{(N-2)}$. However, we must note that: (1) The APS amplitudes vary strongly with the acquisition date, as summer acquisitions are in general noisier than winter acquisitions, and (2) seasonal deformation or residual stratified atmospheric delays break the randomness assumption underlying the uncertainty analysis. We thus compared the velocity maps (Figure S2) obtained by (1) implementing or not one of the approaches used to reduce APS impact, and (2) including or not a seasonal term in the regression analysis.

One approach to reduce the APS effect is to smooth the time series for each pixel by computing the median over a moving window of 10 subsequent radar acquisitions, thus avoiding the least-square regression to be sensitive to strong outliers. The degree of freedom is then reduced to ($\frac{N}{5}$ - 2), although the velocity uncertainty decreases after median filtering (Figure S3). Another approach is to weight each acquisition by the inverse of the global APS amplitude averaged for each date. In the latter case, we cannot compute a velocity uncertainty on the regression analysis. We also include a seasonal term in the form of sine and cosine functions in the parameterization

(see details in the Supporting Information). We find that seasonal signals are large within the study area, possibly due to hydrological loading or to residual tropospheric delays not corrected by the ERA5 model. Phase delay maps for each acquisition were referenced by subtracting the averaged phase of all pixels having the best misclosure RMS values (see details in the Supporting Information) prior to the regression analysis.

The reliability of the retrieved deformation patterns can be assessed by comparing the six different velocity maps in Figure S2. The location and sign of the main patterns are consistent for all maps. However, the amplitude of the LOS velocity anomalies that follow some valleys, such as Sion, Aosta, and Susa Valleys, depends upon the inclusion of a seasonal term and upon the approach used to decrease APS impact. Accordingly, the time series in these valleys contain a clear residual seasonal signal. Furthermore, these valleys display larger velocity uncertainties. Therefore, the velocity patterns along those three valleys can partly be explained by a poorer stratified atmospheric correction, which is based on ERA5 atmospheric variables extrapolated below the ERA5 model elevation (Doin et al., 2009). Figure 1a shows that the aforementioned valleys are the ones displaying the sharpest topographic gradients with respect to the surrounding summits, as well as the sharpest contrasts between valley floors and ERA5 grid node elevations.

InSAR velocities shown in Figures 2a and 2c were finally referenced to published GNSS rates (Kreemer et al., 2020) by adjusting two ramps in azimuth and range and an offset (Supporting Information and Figure S4). Areas moving toward the satellite concern mainly the areas of high topography as well as the foothills of the Alpine chain, while the chain periphery and coastal areas are dominated by motions away from the satellite. The velocity map derived from the median-filtered time series (Figure 2a) displays a higher amplitude range (±3 mm/yr in LOS) than the one retrieved from the APS-weighted time series (±2 mm/yr in LOS, Figure 2c). Velocities around the Po plain correspond to larger uncertainties, suggesting that they are not well modeled by the linear and seasonal parametric decomposition. This is not surprising, as this area is affected by strong and complex seasonal variations, with multi-annual variability. In the central and eastern Po plain, these variations are possibly due to local hydrology variations such as oscillations of the water table (Romagnoli et al., 2003) or hydrologic loading (Richter et al., 2004; Zerbini et al., 2007, 2010, 2013). For the rest of the study, we focus on the velocity map obtained with the APS-weighted time series (Figure 2c), for which we have a slightly better fit to GNSS data (Figure S4).

However, we use the 1-σ uncertainty map associated with the median-filtered time series (Figure 2b).

To better compare the long-wavelength patterns with those retrieved from other studies, we masked pixels with uncertainty values above 0.8 mm/yr according to Figure 2b and then implemented a spatial smoothing with a 20-km-wide Gaussian filter on the map shown in Figure 2c. The smoothed velocity field (Figure 2d and Figure S5) is less affected by non-tectonic effects and is compared to the projected LOS velocities of two GNSS solutions, the one from Kreemer et al. (2020) and the vertical velocity field from Sternai et al. (2019), for which we adjusted the reference frame by adding an offset of +0.25 mm/yr. The InSAR LOS velocities reveal an overall consistency with the GNSS projected velocities derived over longer time series. InSAR and GNSS solutions deviate locally though, mainly in places where the two GNSS solutions also differ from one another (e.g., at OSTA station, Figure 2e). While a few GNSS sites may be affected by local processes or by shorter instrumentation time spans, InSAR rates may suffer from strong residual APS locally or may be affected by potential non-tectonic, e.g. hydrological, multi-annual trends.

The consistency between InSAR and GNSS is emphasized by the three velocity profiles drawn perpendicularly to the strike of the Alpine belt (Figure 2e). They highlight that no systematic correlation is found between elevation and LOS velocities across the chain, even if the area of highest positive velocities correlates with the area of highest topography (Aiguilles Rouges (AR) and Mont-Blanc (MB) areas), in good agreement with GNSS measurements. These results demonstrate that the LOS velocity field derived from 4 years of InSAR data is well-comparable to the longer-term geodetic measurements and is thus representative of the tectonic deformation affecting the Western Alps.

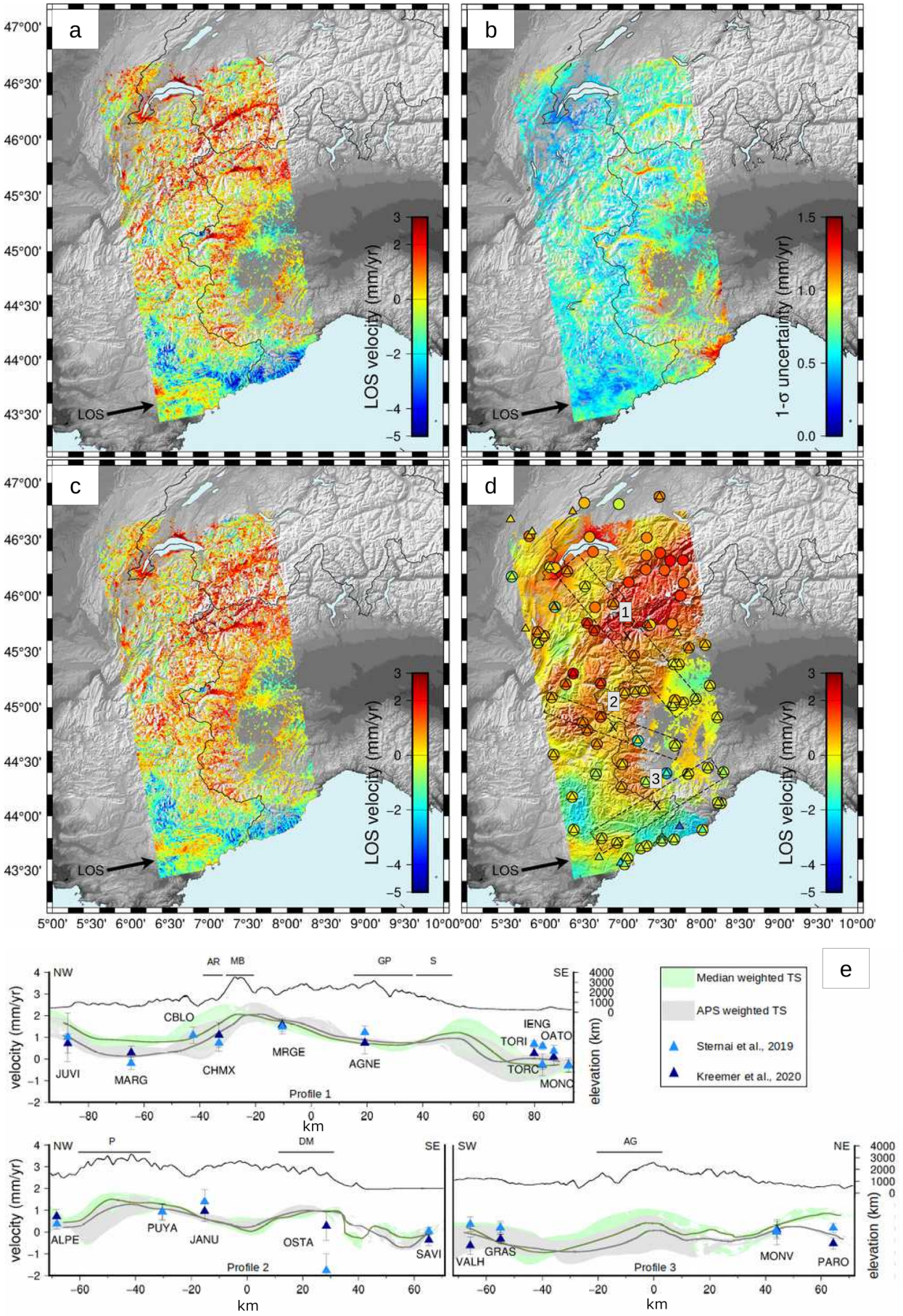
a
b
c
d
e
LOS
LOS velocity (mm/yr)
1-σ uncertainty (mm/yr)
47°00'
46°30'
46°00'
45°30'
45°00'
44°30'
44°00'
43°30'
5°00' 5°30' 6°00' 6°30' 7°00' 7°30' 8°00' 8°30' 9°00' 9°30' 10°00'
1
2
3
Median weighted TS
APS weighted TS
Sternai et al., 2019
Kreemer et al., 2020
velocity (mm/yr)
elevation (km)
km
NW
SE
SW
NE
AR
MB
GP
S
P
DM
AG
JUVI
MARG
CBLO
CHMX
MRGE
AGNE
IENG
TORI
OATO
TORC
MONC
Profile 1
ALPE
PUYA
JANU
OSTA
SAVI
Profile 2
VALH
GRAS
MONV
PARO
Profile 3

Figure 2. LOS velocity maps and profiles. Black arrows west of the track show the satellite-viewing direction. The incidence angle varies from ~ 29° in near range to ~ 41° in far range. Positive/negative velocities represent motions toward/away from the satellite, respectively. **a)** Linear velocity estimated on the median-filtered time series. **b)** 1-σ uncertainty map derived from the error analysis of the time series from a). **c)** Linear velocity estimated on the APS-weighted time series. **d)** Comparison of the smoothed InSAR velocity field derived from the velocity map in c) with GNSS velocities projected in LOS (same scale as InSAR) from Sternai et al., 2019 (circles) and from Kreemer et al., 2020 (triangles). Dashed lines represent the extent of the profiles in e). **e)** InSAR velocity profiles extracted from the median-filtered (green envelopes) and APS-weighted (grey envelopes) time series. Solid curves represent the median of the projected InSAR velocities, solid black lines the topography, and triangles the LOS velocities and 1-σ uncertainties of the GNSS solutions from d). Acronyms refer to the geological features displayed in Figure 3c.

4 Discussion: uplift localization

We make here the first-order assumption that the LOS velocities unraveled by this study mostly represent vertical motions. This is due to (1) the low viewing angle of the satellite from the vertical, which is varying from 29.16° to the west to 41.85° to the east, (2) the very small amplitude of the horizontal deformation across the Western Alps (around 15 nanostrain/yr of extension, see Nocquet et al., 2016; Walpersdorf et al., 2018), and (3) the removal from the velocity map of the majority of DSGSD features, which contain significant horizontal motion. In the following, we will therefore display and discuss the velocity field converted to vertical using local incidence angles.

Figure 3 displays a comparison of the corresponding vertical InSAR-derived velocity field with a set of features derived from previous Alpine studies. Figure 3a presents the ice extent corresponding to the Last Glacial Maximum (LGM, c.a. 18-20 ka) simplified from Ehlers and Gibbard (2004). As already pointed out by Sternai et al. (2019), the area of glacial extent matches at first order the region of uplift. Reciprocally, subsidence along the coast and in the Nice foreland would correspond to the foreland of LGM ice cover. Beside the first order agreement of geodetic uplift with LGM extent already observed in previous studies, we note that two uplifting massifs, the Pelvoux and the Argentera ones, are apparently not well colocated with the LGM ice extent.

Figure 2d reveals that no GNSS data are available in the inner Pelvoux massif, while GNSS stations indicate either low uplift or null motion in the Argentera massif. Some deglaciation models predict measurable uplift rates of the Pelvoux massif, such as Barletta's (2006) models of uplift rates due to deglaciation following the Little Ice Age (LIA, 18th-19th c., Figure 3a) and due to present-day glacier shrinkage (Figure 3b). The rates predicted by these models remain very low (locally up to 0.3 and 0.2 mm/yr, respectively) compared to the rates derived from geodesy, and their magnitude is hardly constrained, especially for the LIA rebound model (Barletta et al., 2006). Nevertheless, the spatial variations they feature are more robust (Barletta et al., 2006) and highlight a differential uplift in the Pelvoux massif with respect to the surrounding areas. The LGM rebound can explain up to 10 to 30 % of uniformly distributed uplift rate in the Western Alps according to various models (Sternai et al., 2019; Stocchi et al., 2005, Barletta et al., 2006). On the contrary, uplift rates due to LIA and present-day glacier shrinkage are lower (~6 to 10 % and ~4% to 12% respectively of the maximum observed uplift rates, Barletta et al., 2006; Sternai et al., 2019), but their modeled spatial variations are in better agreement with those imaged here by InSAR.

When the InSAR-derived velocities are compared to the main crystalline massifs of the Alps (Figure 3c), it becomes obvious that uplift is limited to the geological Alpine belt, affecting both its external and internal massifs (AA to P in Figure 3c). Our results show a marked uplift pattern extending in the higher-elevation areas, especially along the Aar-Mont-Blanc-Belledonne axis, that was previously identified with geodetic measurements but at a lower resolution (Figure 2d; Nocquet et al., 2016; Walpersdorf et al., 2018; Masson et al., 2019; Sanchez et al., 2019). Our InSAR velocity field moreover reveals other areas with sharp contours of relative uplift to the south of this axis, for which spatial correlation with geological features (Pelvoux and Argentera massifs) could not be previously established based on GNSS measurements. We further compare InSAR velocities to exhumation rates estimated from thermochronometric ages in the Western Alps (Figure 3d; Fox et al., 2015). The Pelvoux and the Argentera massifs display young Apatite fission track ages similar to those retrieved in the Aar, Mont-Blanc, Belledonne and Aiguilles-Rouges massifs. The corresponding exhumation rates are above 1 mm/yr, which is 25% to 50% more than in the surroundings. Other studies show that these crystalline massifs are associated with important erosion rates. For instance, the postglacial erosion model derived from sediment distribution in Mey et al (2016) also displays higher erosion rates in the Argentera and Pelvoux massifs than in the surroundings. The observed coincidence of larger uplift rates, larger

exhumation rates and larger erosion rates in crystalline massifs points towards retroaction mechanisms that help focus the vertical crustal response to external solicitations (erosional, glacial or slab unloading) or to internal buoyancy forces, in the absence of dominant horizontal convergence. This coincidence suggests that focused uplift is aided by inherited crustal weak features, faults or shear zones, or rheological heterogeneities (e.g. Herwegh et al., 2020).

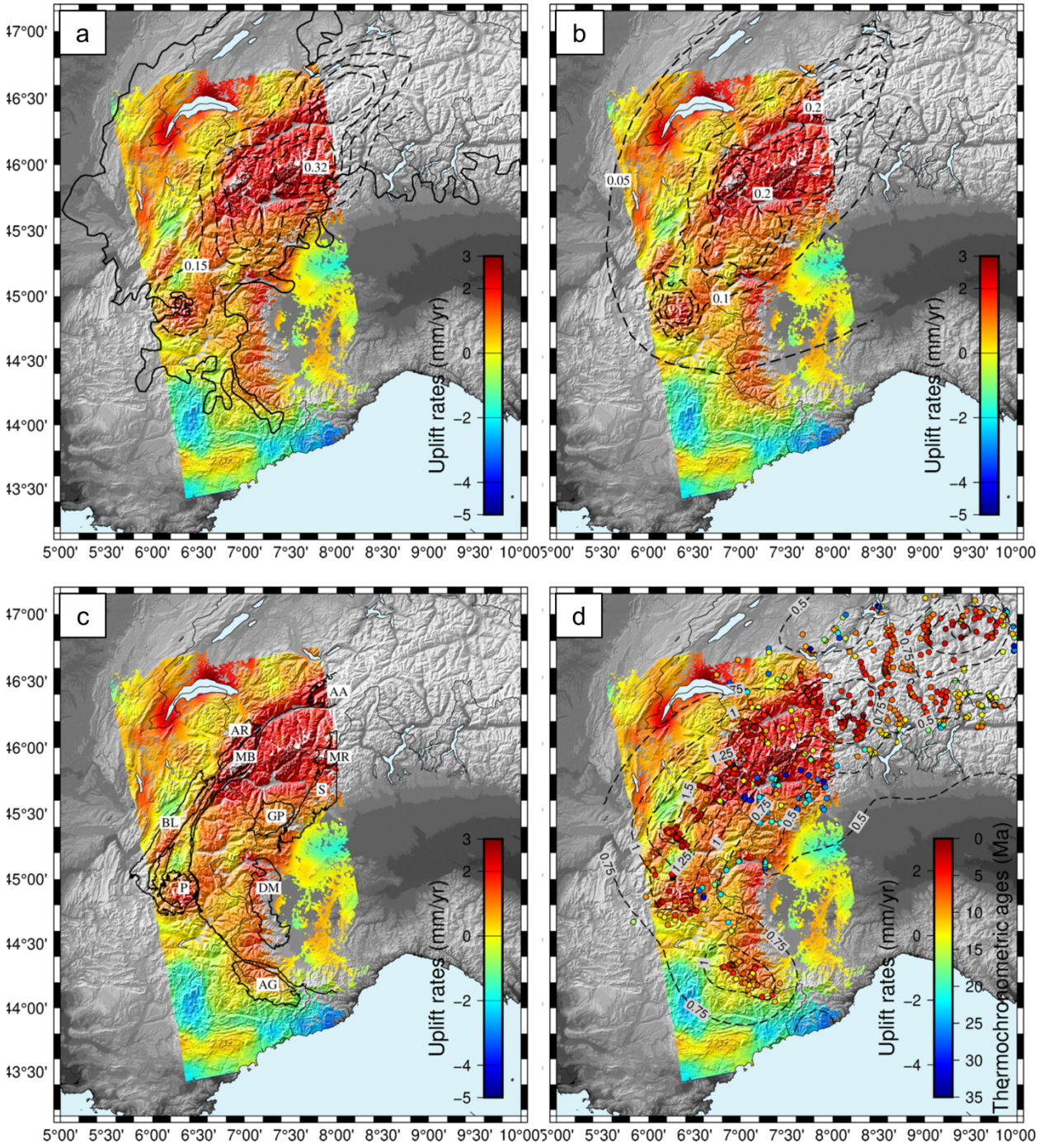

Figure 3. Comparison of the vertical-converted velocity map with: **a)** LGM extent (solid black line) from Ehlers and Gibbard (2004) and LIA-induced uplift rates (dashed isolines, mm/yr) modeled by Barletta et al. (2006); **b)** uplift rates induced by present-day glacier shrinkage (dashed isolines, mm/yr) modelled by Barletta et al. (2006); **c)** geological units (crystalline massifs) modified from Sue et al. (1999): AA=Aar, AG=Argentera, AR=Aiguilles-Rouges, BL=Belledonne, DM=Dora Maira, GP=Gran Paradiso, MB=Mont-Blanc, MR=Monte Rosa, P=Pelvoux, S=Sesia ; and **d)** Thermochonometric ages (colored circles) and corresponding exhumation rates (dashed isolines, mm/yr) shown in Fox et al. (2015).

5 Conclusions

This study provides the first velocity field derived by a multi-temporal InSAR analysis at the scale of the Western Alps. The retrieved regional patterns are in good agreement with GNSS measurements, displaying uplift at the center of the belt with a maximum localized on the higher-elevation parts of the belt, associated with subsidence at the periphery. Moreover, we improved the spatial resolution of the global uplift pattern derived from interpolated GNSS data. We observed that the maximum of uplift is localized along the Aar-Mont-Blanc axis, and that short-wavelength spatial variations of the uplift pattern appear correlated with geological crystalline massifs in the southern part of the Western Alps. Measured geodetic uplift rates are provided in the inner Pelvoux massif for the first time. These geodetic uplift patterns moreover mimic exhumation patterns derived on geological timescales (~5Ma, Fox et al., 2015).

The relative uplift-rate contribution arising from each process affecting the belt today is a matter of debate (Sternai et al., 2019). It nevertheless appears that the spatial variability observed in the uplift pattern cannot be only induced by the LGM rebound, which acts on much larger wavelengths than the ones observed in this study (Barletta et al., 2006; Persaud & Pfiffner, 2004; Schlatter et al., 2005). It requires either additional processes acting at smaller wavelengths and/or differential localization mechanisms allowing large-scale processes to induce a more localized surficial response, in the presence of rheological or inherited lithospheric structural heterogeneities. Isostatic adjustment to LIA and present-day ice mass losses is likely to be included in these short-wavelength additional processes, as well as erosion and drainage. Larger-scale possible driving processes involve the crust buoyancy, the slab pull or detachment beneath the

chain associated with the end of the convergence between Africa and Eurasia in the Western Alps. Beyond this undoubted complexity, this study points out the importance of InSAR measurements in low-deforming areas. Such measurements allow enhancing the spatial resolution of the derived ground motions, thus providing important elements for further analyzing the complex interactions between driving forces and the heterogeneous response of the lithosphere.

Acknowledgments

This work was funded by the OSUG@2020 LabEx (Investissements d'avenir - ANR10LABX56) and by the IRSN (Institut de Radioprotection et de Sûreté Nucléaire). It was also supported by the Programme National de Télédétection Spatiale (PNTS). The Sentinel-1 data are available at https://scihub.copernicus.eu/dhus/. The InSAR velocity solutions are available at https://doi.org/10.5281/zenodo.5763672. This work was made possible thanks to the CIMENT/GRICAD infrastructure (https://gricad.univ-grenoble-alpes.fr). We would like to thank B. Goffé for fruitful discussions, and M. Fox and P. Sternai for making the exhumation data and GNSS data available respectively. The GNSS solution from Kreemer et al. (2020) is distributed online (doi:10.7910/DVN/ONATFP). We thank the editor, M. Shirzaei and an anonymous reviewer for their helpful comments.

References

Agliardi, F., Crosta, G., & Zanchi, A. (2001). Structural constraints on deep-seated slope deformation kinematics. Engineering Geology, 59(1–2), 83–102.

Andre, P. (2020). Measurement of the Alps deformation by radar interferometry: large-scale inventory of deep-seated gravitational slope deformations. Grenoble: ISTerre, Grenoble University. Retrieved from Master thesis.

Ansari, H., De Zan, F., & Parizzi, A. (2020). Study of systematic bias in measuring surface deformation with SAR interferometry.

Aslan, G., Foumelis, M., Raucoules, D., De Michele, M., Bernardie, S., & Cakir, Z. (2020). Landslide mapping and monitoring using persistent scatterer interferometry (PSI) technique in the French Alps. Remote Sensing, 12(8), 1305.

Barletta, V. R., Ferrari, C., Diolaiuti, G., Carnielli, T., Sabadini, R., & Smiraglia, C. (2006). Glacier shrinkage and modeled uplift of the Alps. Geophysical Research Letters, 33(14).

https://doi.org/10.1029/2006GL026490

Blondeau, S., Gunnell, Y., & Jarman, D. (2021). Rock slope failure in the Western Alps: A first comprehensive inventory and spatial analysis. Geomorphology, *380*, 107622.https://doi.org/10.1016/j.geomorph.2021.107622

Biggs, J., Wright, T., Lu, Z., & Parsons, B. (2007). Multi-interferogram method for measuring interseismic deformation: Denali Fault, Alaska. Geophysical Journal International, 170(3), 1165-1179.

Calais, E., Nocquet, J.-M., Jouanne, F., & Tardy, M. (2002). Current strain regime in the Western Alps from continuous Global Positioning System measurements, 1996–2001. Geology, 30(7), 651-654.

Coward, M., & Dietrich, D. (1989). Alpine tectonics—An overview. Geological Society, London, Special Publications, 45(1), 1–29.

Daout, S., Doin, M.-P., Peltzer, G., Socquet, A., & Lasserre, C. (2017). Large-scale InSAR monitoring of permafrost freeze-thaw cycles on the Tibetan Plateau. Geophysical Research Letters, 44(2), 901–909. https://doi.org/10.1002/2016GL070781

Daout, S., Sudhaus, H., Kausch, T., Steinberg, A., & Dini, B. (2019). Interseismic and Postseismic Shallow Creep of the North Qaidam Thrust Faults Detected with a Multitemporal InSAR Analysis. Journal of Geophysical Research: Solid Earth, 124(7), 7259–7279. https://doi.org/10.1029/2019JB017692

De Zan, F., & Gomba, G. (2018). Vegetation and soil moisture inversion from SAR closure phases: First experiments and results. Remote sensing of environment, 217, 562-572.

Doin, M. P., Lasserre, C., Peltzer, G., Cavalié, O., & Doubre, C. (2009). Corrections of stratified tropospheric delays in SAR interferometry: Validation with global atmospheric models. Journal of Applied Geophysics, 69(1), 35–50.

Doin, M.-P., Guillaso, S., Jolivet, R., Lasserre, C., Lodge, F., Ducret, G., & Grandin, R. (2011). Presentation of the small baseline NSBAS processing chain on a case example: the Etna deformation monitoring from 2003 to 2010 using Envisat data. In Proceedings of the Fringe symposium (pp. 3434–3437).

Doin, M.-P., Twardzik, C., Ducret, G., Lasserre, C., Guillaso, S., & Jianbao, S. (2015). InSAR measurement of the deformation around Siling Co Lake: Inferences on the lower crust viscosity in central Tibet. Journal of Geophysical Research: Solid Earth, 120(7), 5290–5310. https://doi.org/10.1002/2014JB011768

Drouillas, Y., Lebourg, T., Zerathe, S., Hippolyte, J. C., Chochon, R., Vidal, M., & Besso, R. (2020). Alpine deep-seated gravitational slope deformation and the Messinian Salinity Crisis. Landslides. https://doi.org/10.1007/s10346-020-01504-5

Ehlers, J., & Gibbard, P. L. (2004). Quaternary glaciations-extent and chronology: part I: Europe. Elsevier.

Elliott, J. R., Biggs, J., Parsons, B., & Wright, T. J. (2008). InSAR slip rate determination on the Altyn Tagh Fault, northern Tibet, in the presence of topographically correlated atmospheric delays. Geophysical Research Letters, 35(12).

Farr, T. G., Rosen, P. A., Caro, E., Crippen, R., Duren, R., Hensley, S., Kobrick, M., Paller, M., Rodriguez, E., Roth, L., & others. (2007). The shuttle radar topography mission. Reviews of geophysics, 45(2).

Fox, M., Herman, F., Kissling, E., & Willett, S. D. (2015). Rapid exhumation in the Western Alps driven by slab detachment and glacial erosion. Geology, 43(5), 379–382.

Grandin, R., Doin, M.-P., Bollinger, L., Pinel-Puysségur, B., Ducret, G., Jolivet, R., & Sapkota, S. N. (2012). Long-term growth of the Himalaya inferred from interseismic InSAR measurement. Geology, 40(12), 1059–1062. https://doi.org/10.1130/G33154.1

Hammond, W. C., Blewitt, G., Li, Z., Plag, H.-P., & Kreemer, C. (2012). Contemporary uplift of the Sierra Nevada, western United States, from GPS and InSAR measurements. Geology, 40(7), 667–670. https://doi.org/10.1130/G32968.1

Hanssen, R. F. (2001). Radar interferometry: data interpretation and error analysis (Vol. 2). Springer Science & Business Media.

Hersbach, H., Bell, B., Berrisford, P., Hirahara, S., Horányi, A., Muñoz-Sabater, J., et al. (2020). The ERA5 global reanalysis. Quarterly Journal of the Royal Meteorological Society.

Herwegh, M., Berger, A., Glotzbach, C., Wangenheim, C., Mock, S., Wehrens, P., et al. (2020).

Late stages of continent-continent collision: Timing, kinematic evolution, and exhumation of the Northern rim (Aar Massif) of the Alps. Earth-Science Reviews, 200, 102959.

Hippolyte, J.-C., Tardy, M., & Nicoud, G. (2006). Recent fault scarps at the Grands-Moulins (Savoy) reveal a major deep seated gravitational spreading (Sackung) in the French Alps. Comptes Rendus Geoscience, 338(10), 734–741.

Hungr, O., Leroueil, S., & Picarelli, L. (2014). The Varnes classification of landslide types, an update. Landslides, 11(2), 167–194.

Jolivet, R., Grandin, R., Lasserre, C., Doin, M.-P., & Peltzer, G. (2011). Systematic InSAR tropospheric phase delay corrections from global meteorological reanalysis data. Geophysical Research Letters, 38(17). https://doi.org/10.1029/2011GL048757

Kreemer, C., Blewitt, G., & Davis, P.M. (2020). Geodetic evidence for a buoyant mantle plume beneath the Eifel volcanic area, NW Europe. Geophysical Journal International, 222(2), 1316–1332.

Masson, C., Mazzotti, S., Vernant, P., & Doerflinger, E. (2019). Extracting small deformation beyond individual station precision from dense Global Navigation Satellite System (GNSS) networks in France and western Europe. Solid Earth, 10(6), 1905–1920. https://doi.org/10.5194/se-10-1905-2019

Mey, J., Scherler, D., Wickert, A. D., Egholm, D. L., Tesauro, M., Schildgen, T. F., & Strecker, M. R. (2016). Glacial isostatic uplift of the European Alps. Nature Communications, 7(1), 13382. https://doi.org/10.1038/ncomms13382

Nocquet, J.-M., Sue, C., Walpersdorf, A., Tran, T., Lenôtre, N., Vernant, P., et al. (2016). Present-day uplift of the western Alps. Scientific Reports, 6(1), 28404. https://doi.org/10.1038/srep28404

Peter, H., Jäggi, A., Fernández, J., Escobar, D., Ayuga, F., Arnold, D., ... & Féménias, P. (2017). Sentinel-1A–First precise orbit determination results. Advances in space research, 60(5), 879-892.

Persaud, M., & Pfiffner, O.-A. (2004). Active deformation in the eastern Swiss Alps: post-glacial faults, seismicity and surface uplift. Tectonophysics, 385(1–4), 59–84.

Pinel-Puysségur, B., Michel, R., & Avouac, J.-P. (2012). Multi-link InSAR time series: Enhancement of a wrapped interferometric database. IEEE Journal of Selected Topics in Applied

Earth Observations and Remote Sensing, 5(3), 784–794.

Richter, B., Zerbini, S., Matonti, F., & Simon, D. (2004). Long-term crustal deformation monitored by gravity and space techniques at Medicina, Italy and Wettzell, Germany. Journal of Geodynamics, 38(3), 281–292. https://doi.org/10.1016/j.jog.2004.07.013

Romagnoli, C., Zerbini, S., Lago, L., Richter, B., Simon, D., Domenichini, F., et al. (2003). Influence of soil consolidation and thermal expansion effects on height and gravity variations. Journal of Geodynamics, 35(4–5), 521–539.

Sánchez, L., Völksen, C., Sokolov, A., Arenz, H., & Seitz, F. (2018). Present-day surface deformation of the Alpine region inferred from geodetic techniques. Earth System Science Data, 10(3), 1503-1526.

Scheiber, R., & Moreira, A. (2000). Coregistration of interferometric SAR images using spectral diversity. IEEE Transactions on Geoscience and Remote Sensing, 38(5), 2179–2191.

Schlatter, A., Schneider, D., Geiger, A., & Kahle, H.-G. (2005). Recent vertical movements from precise levelling in the vicinity of the city of Basel, Switzerland. International Journal of Earth Sciences, 94(4), 507–514.

Schmid, S., & Kissling, E. (2000). The arc of the western Alps in the light of geophysical data on deep crustal structure. Tectonics, 19(1), 62–85.

Serpelloni, Enrico, Pintori, F., Gualandi, A., Scoccimarro, E., Cavaliere, A., Anderlini, L., Belardinelli, M. E., & Todesco, M. (2018). Hydrologically induced karst deformation : Insights from GPS measurements in the adria-eurasia plate boundary zone. Journal of Geophysical Research: Solid Earth, 123(5), 4413–4430.

Serpelloni, Enrico, Vannucci, G., Anderlini, L., & Bennett, R. A. (2016). Kinematics, seismotectonics and seismic potential of the eastern sector of the European Alps from GPS and seismic deformation data. Tectonophysics, 688, 157–181.

Singh, L. P., Van Westen, C. J., Ray, P. C., & Pasquali, P. (2005). Accuracy assessment of InSAR derived input maps for landslide susceptibility analysis: a case study from the Swiss Alps. Landslides, 2(3), 221-228.

Sternai, P., Sue, C., Husson, L., Serpelloni, E., Becker, T. W., Willett, S. D., et al. (2019). Present-

day uplift of the European Alps: Evaluating mechanisms and models of their relative contributions. Earth-Science Reviews, 190, 589–604. https://doi.org/10.1016/j.earscirev.2019.01.005

Stocchi, P., Spada, G., & Cianetti, S. (2005). Isostatic rebound following the Alpine deglaciation: impact on the sea level variations and vertical movements in the Mediterranean region. Geophysical Journal International, 162(1), 137–147. https://doi.org/10.1111/j.1365-246X.2005.02653.x

Sue, C. (2020). Late-Orogenic Extension and Current Tectonics in the Western and Central Alps: a Review.

Sue, Christian, Thouvenot, F., Fréchet, J., & Tricart, P. (1999). Widespread extension in the core of the western Alps revealed by earthquake analysis. Journal of Geophysical Research: Solid Earth, 104(B11), 25611–25622. https://doi.org/10.1029/1999JB900249

Walpersdorf, A., Pinget, L., Vernant, P., Sue, C., Deprez, A., & the RENAG team. (2018). Does Long-Term GPS in the Western Alps Finally Confirm Earthquake Mechanisms? Tectonics, 37(10), 3721–3737. https://doi.org/10.1029/2018TC005054

Zebker, H. A., Rosen, P. A., & Hensley, S. (1997). Atmospheric effects in interferometric synthetic aperture radar surface deformation and topographic maps. Journal of Geophysical Research: Solid Earth, 102(B4), 7547-7563.

Zerbini, S., Richter, B., Rocca, F., Dam, T. van, & Matonti, F. (2007). A Combination of Space and Terrestrial Geodetic Techniques to Monitor Land Subsidence: Case Study, the Southeastern Po Plain, Italy. Journal of Geophysical Research: Solid Earth, 112(B5). https://doi.org/10.1029/2006JB004338

Zerbini, S., Raicich, F., Richter, B., Gorini, V., & Errico, M. (2010). Hydrological signals in height and gravity in northeastern Italy inferred from principal components analysis. Journal of Geodynamics, 49(3), 190–204. https://doi.org/10.1016/j.jog.2009.11.001

Zerbini, S., Raicich, F., Errico, M., & Cappello, G. (2013). An EOF and SVD analysis of interannual variability of GPS coordinates, environmental parameters and space gravity data. Journal of Geodynamics, 67, 111–124. https://doi.org/10.1016/j.jog.2012.04.006

Geophysical Research Letters

Supporting Information for

Spatial Heterogeneity of Uplift Pattern in the Western European Alps Revealed by InSAR Time Series Analysis

M. Mathey[1], M.-P. Doin[1], P. André[1], A. Walpersdorf[1], S. Baize[2], C. Sue[1,3]

[1]University Grenoble Alpes, University Savoie Mont Blanc, CNRS, IRD, IFSTTAR, ISTerre, Grenoble, 38000, France.

[2]2IRSN,PSE-ENV/SCAN/BERSSIN, BP 17, Fontenay-aux-roses, F-92262, France.

[3]Chrono-Environnement Besançon, OSU THETA, University Bourgogne-Franche-Comté,

Besançon, 25000, France.

Contents of this file

Additional Supporting Information (Files uploaded separately)

ZIP file with InSAR raw and smoothed final velocity solution values

Details on post-processing choices

Quality measurement and masking steps.

Several quality indices allow to mask pixels after the time series inversion procedure. We first use the root mean square (RMS) of the network misclosure residuals in the time series inversion. As unwrapping errors have been corrected or masked, the final RMS value depends mainly on the temporal coherence of pixels. The RMS thus increases for pixels affected by vegetation changes or unmasked seasonal snow coverage. Here, we choose to mask out pixels with RMS values above 0.5 radians (Figure S1a).

The second criterion is the "Misclosure of Low Duration Interferograms", MLDI, which is defined as the average signed misclosure residual of all low duration interferograms in the time series inversion of the interferometric network. Indeed, in the inversion, two months to one year interferograms effectively counterbalance the potential biases introduced by short (< one month) temporal baseline interferograms (De Zan et Gomba, 2018; Ansari et al., 2020). Negative MLDI values point toward pixels with potential negative biais, which can result in a velocity artificially indicating subsidence. Inversely, positive MLDI occurs where the biais could produce false uplift. Here, we use the average difference between reconstructed and input 18-days interferograms, with a 0.1 radians threshold, to symmetrically mask out potentially biased areas (Figure S1b). These masked areas appear in agricol plains (crops, as in the Po plain) for negative bias or in very limited forest areas (for positive bias, less important). In addition to this criterion, we also masked pixels which have been unwrapped mostly on short duration interferograms, for two reasons: (1) the MLDI criterium is less effective if less long-duration interferograms are present, (2) Relative to other pixels, these pixels present worse long-duration coherence (e.g., one year interferograms are not coherent), and are thus more likely to be affected by a bias. The criterion is defined as the averaged temporal baseline of interferograms unwrapped for a given pixel. The threshold is set at 0.102 year (Figure S1c). We also compared our inversion results to the results of inversions without 6 days interferograms to evaluate the difference in the estimated cumulative displacements, which appears negligible in unmasked areas.

Last, we choose to mask pixels falling within polygons of identified gravitational slope deformation (Figure S1d). Rapid landslides are unlikely to appear in the velocity map since they produce a high temporal decorrelation and are not well unwrapped; however DSGSD reach velocities of the order of 15 mm/yr at the maximum in the Alps (Andre, 2020). If these features are related to much shorter wavelengths than the surface deformation investigated in this study, their inclusion in the velocity map could lead to erroneous velocity estimates when filtering the velocity map to get the smoothed velocity field. The velocity maps presented in the main paper as well as in the following sections are masked according to these four criteria.

Velocity estimates

To compute the velocity, we estimate a linear term in the displacement time series. This linear term can be estimated as the only component of pixel displacement and retrieved through an Ordinary Least Square (OLS) regression, or it can be dissociated from a seasonal component through a multilinear regression. In this case, two additional functions, a sinusoidal and a cosinus, are used to separate seasonal and linear signals and the displacement y(t) of each pixel is described as the time function :

$$y(t) = a*t+b+C1*\cos(2\pi*t)+C2*\sin(2\pi*t) \quad (1)$$

Where t is time, a is the amplitude of the linear term, b is a constant and C1 and C2 are the amplitudes of seasonal signals. The first two terms (in blue) are the only ones considered in the OLS case. In both cases, we invert for the amplitude of each basis function.

The linear term can be computed either on the raw displacement time series, or once the time series have been corrected from outliers. The weight of outlier values can be reduced using a sliding median on consecutive dates. Alternatively, the averaged amplitude of the residual APS for each time step can be computed by least square summing of the residual to the regression. This APS amplitude, which is statistically much higher in summer than in winter can be used to downweight dates with strong atmospheric perturbations.

The corresponding estimated velocities, for each combination of the two possible regression procedures on the raw, APS weighted or median filtered time series, are displayed on Figure S2. At the individual pixel scale, the separation of linear and seasonal terms appears necessary to better describe the displacements through time, even if at the scale of the study area, the difference between linear estimation alone and linear with seasonal estimation appears really significant only on the Po plain and along some alpine valleys. Overall, the amplitudes vary slightly between each velocity map but the positive and negative patterns remain consistent, except along three main valleys (Sion, Susa and Aosta valleys) that are further analyzed in the main text. The velocity solution retained is the one resulting from APS residual weighting of time series (Figure S2d). Since the latter is not known a priori and results from an iterative inversion procedure, we estimated the uncertainties on the velocities as standard errors on the regression to the time series sliding median. While reducing the number of independent observations, the sliding window median computation leads to a significant decrease of the associated uncertainties compared to the ones estimated on the raw time series (Figure S3).

Comparison with GPS and ramp estimation

InSAR velocity maps derived from the present analysis have no residual ramp in range and azimuth and have been on average set to zero in areas with low RMS values. In order to provide a common reference for the velocity maps and GNSS data, we adjusted three parameters, a constant aGPS, a coefficient in range bGPS, and a coefficient in azimuth cGPS to the difference between the InSAR LOS velocity map and GPS velocity projected along LOS:

vGPS - vinsar = aGPS + bGPS*range + cGPS*azimuth (2)

We choose to use the GNSS solution from Kreemer et al. (2020) and InSAR velocity extracted from the filtered map shown in Figure 2d at GNSS locations. We first subtracted, from the GPS velocity field in the IGS14 reference frame, the mean horizontal velocity in our area of interest. GPS data with residual horizontal motions along East and North directions larger than 1.9 times their respective standard deviations (0.95 and 1.16 mm/yr, respectively) were discarded for the adjustment. Finally, 63 remaining common GPS and InSAR LOS velocity measurements, associated with GPS LOS uncertainties, were used to adjust aGPS, bGPS and cGPS. The InSAR velocity field set in a common reference frame with the GPS data is then obtained as:

Vinsar ref = Vinsar + aGPS + bGPS*range + cGPS*azimuth (3)

Figure S4 displays the referenced InSAR velocities as a function of GPS velocities in LOS from Kreemer et al., 2020, together with a distribution of the velocity difference. The correlation coefficient is 0.63 and the standard deviation of velocity differences is as low as 0.8 mm/yr, showing a good agreement considering the uncertainties associated with both data sets.

The vertical GNSS solution of Sternai et al. (2019), projected into LOS, then needed an adjustment of +0.25 mm/yr in order to fit this common reference frame.

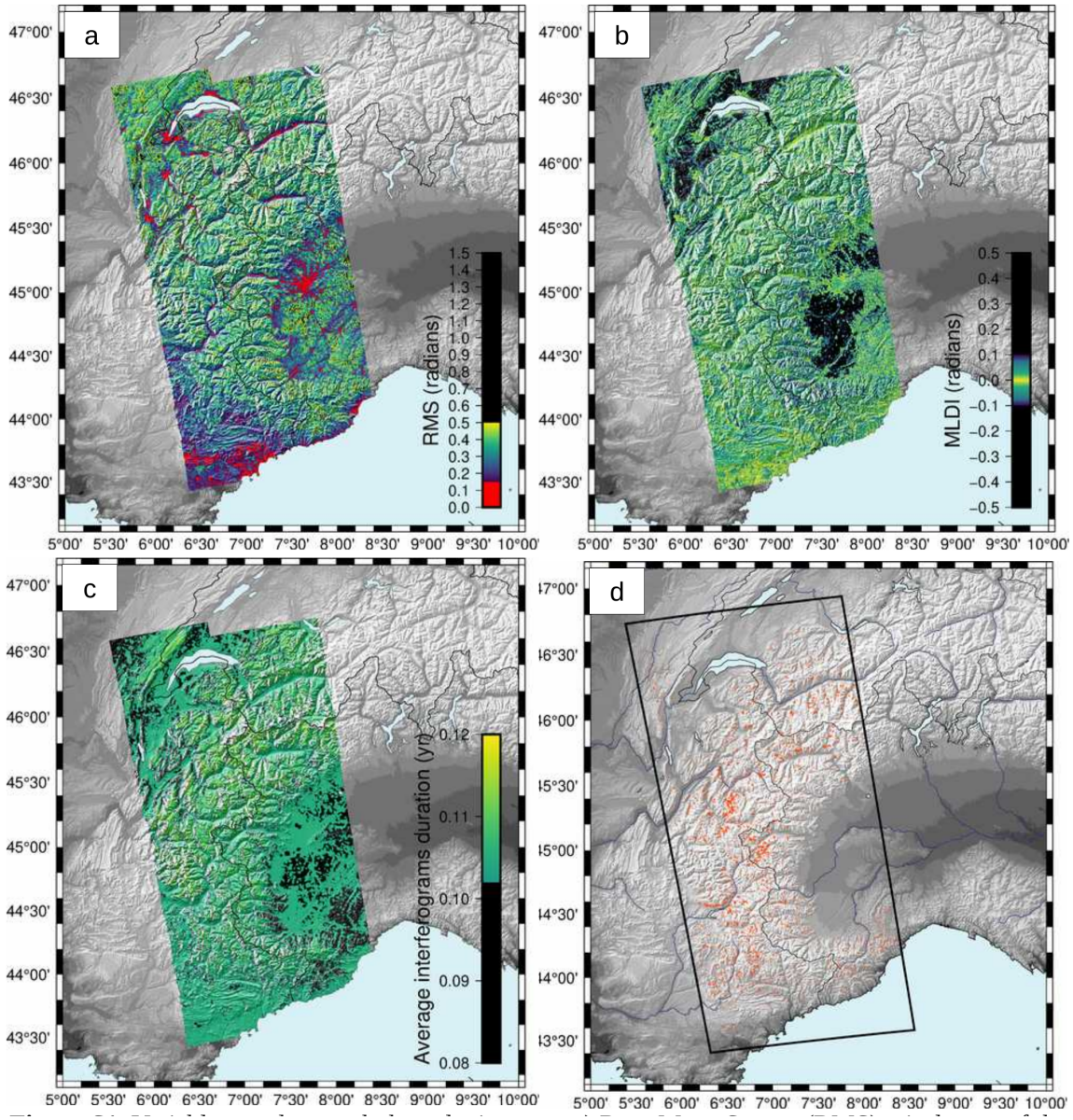

Figure S1. Parameters used to mask the velocity map. a) Root Mean Square (RMS) misclosure. Red areas (lowest RMS values) represent the pixels used for the distributed referencing of the velocity map (velocities are expressed relatively to these pixels). Black areas (not numerous) represent pixels of highest RMS values. These pixels are characterized by high temporal decorrelation and are masked from the velocity map. White pixels correspond to areas that could not be unwrapped due to highest temporal decorrelation (glacier areas or highest summits). b) Averaged network Misclosure of Low Duration Interferograms (MLDI). Pixels of large MLDI (dark pixels) correspond to agricultural areas or to mountain foothills and were masked from the velocity map. c) Average of interferograms temporal baseline for each pixel.

Pixels with values lower than 0.102 year were masked out from the velocity map. d) Map of the Deep-Seated Gravitational Slope Deformation (DSGSD) landslides (red pixels) affecting the processed area (black polygon). These features were identified through a combined slope and velocity analysis by Andre (2020). The corresponding pixels are masked from the velocity map.

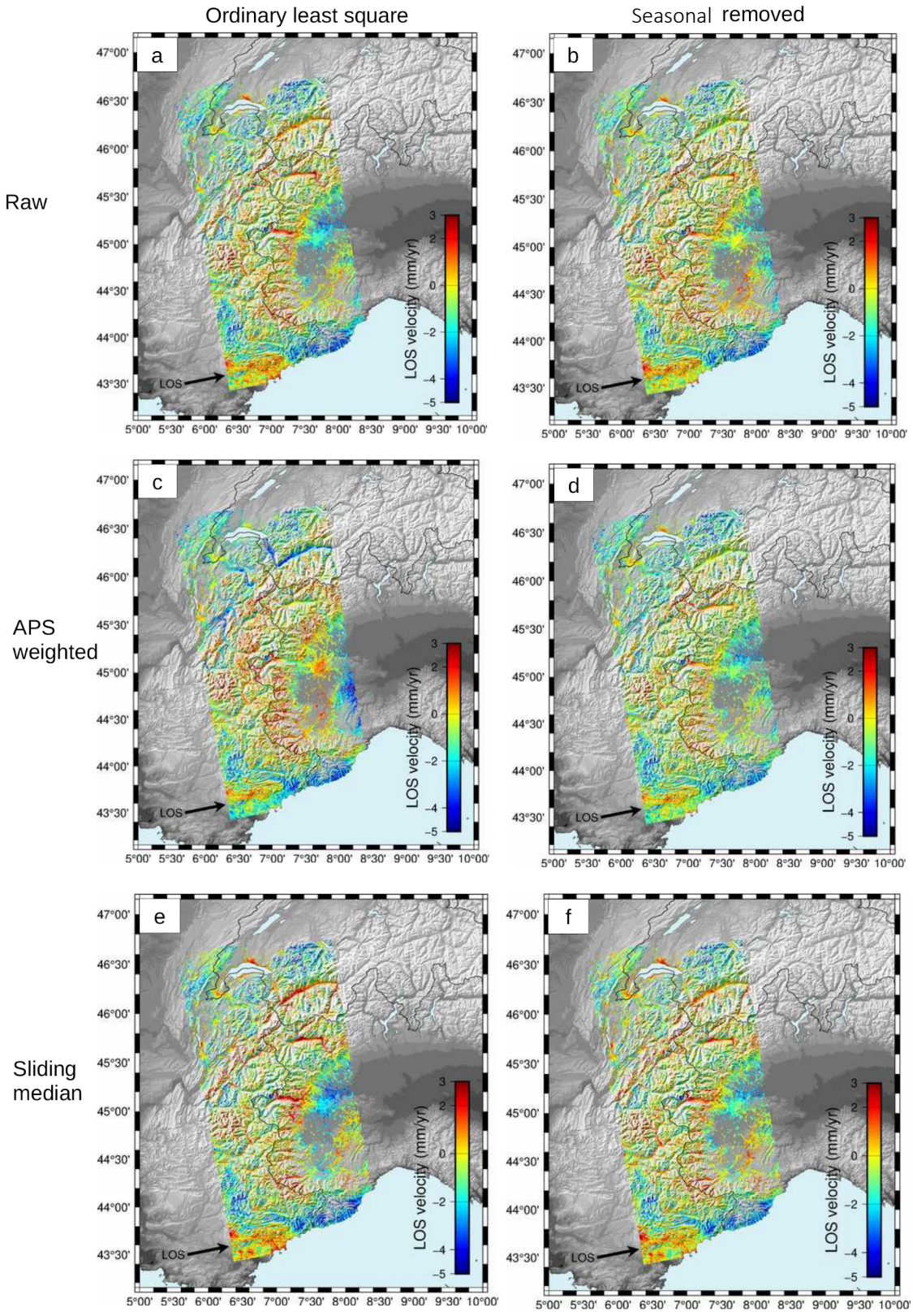
Ordinary least square
Seasonal removed
Raw
APS weighted
Sliding median
a
b
c
d
e
f
LOS
LOS velocity (mm/yr)
47°00'
46°30'
46°00'
45°30'
45°00'
44°30'
44°00'
43°30'
5°00' 5°30' 6°00' 6°30' 7°00' 7°30' 8°00' 8°30' 9°00' 9°30' 10°00'
3
2
0
−2
−4
−5

Figure S2. Post-processing of the time series to derive velocity maps. a), c), and e): Ordinary least square estimation of the velocity on the raw time series, on the APS weighted time series, and on the sliding median of the time series respectively. b), d), and f): Joint estimation of the velocity and of the seasonal signal on raw time series, APS weighted time series, and sliding median time series, respectively. The velocity maps shown here are not referenced to GNSS data yet.

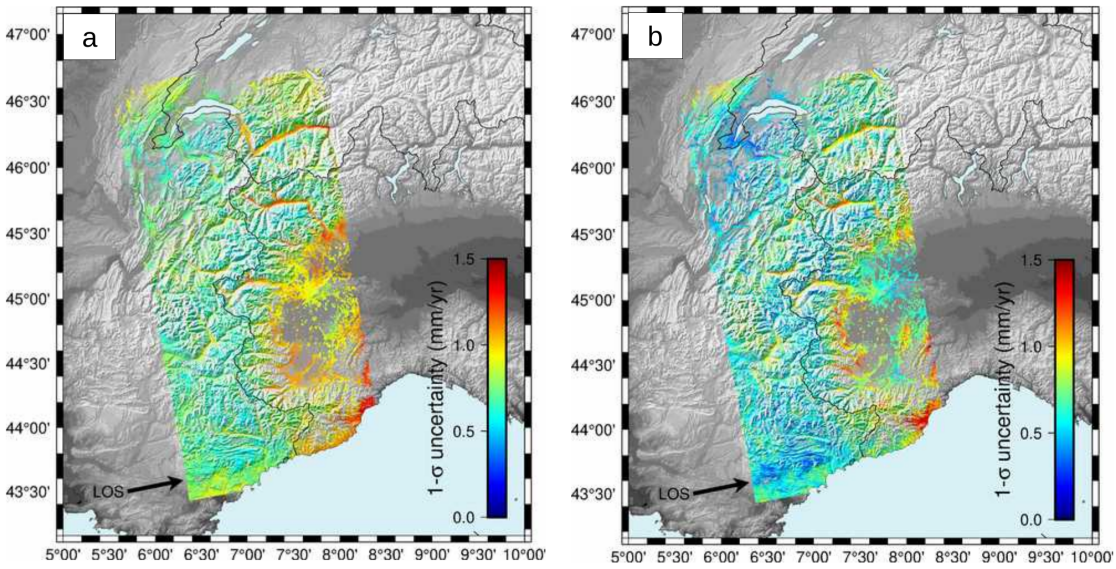

Figure S3. Error maps (mm/yr) on the velocity in line of sight derived from the standard error analysis of a) the raw times series (Figure 2b)) and of b) the sliding median filtered time series (Figure 2f)). In both cases, the seasonal signal is jointly estimated with the linear term.

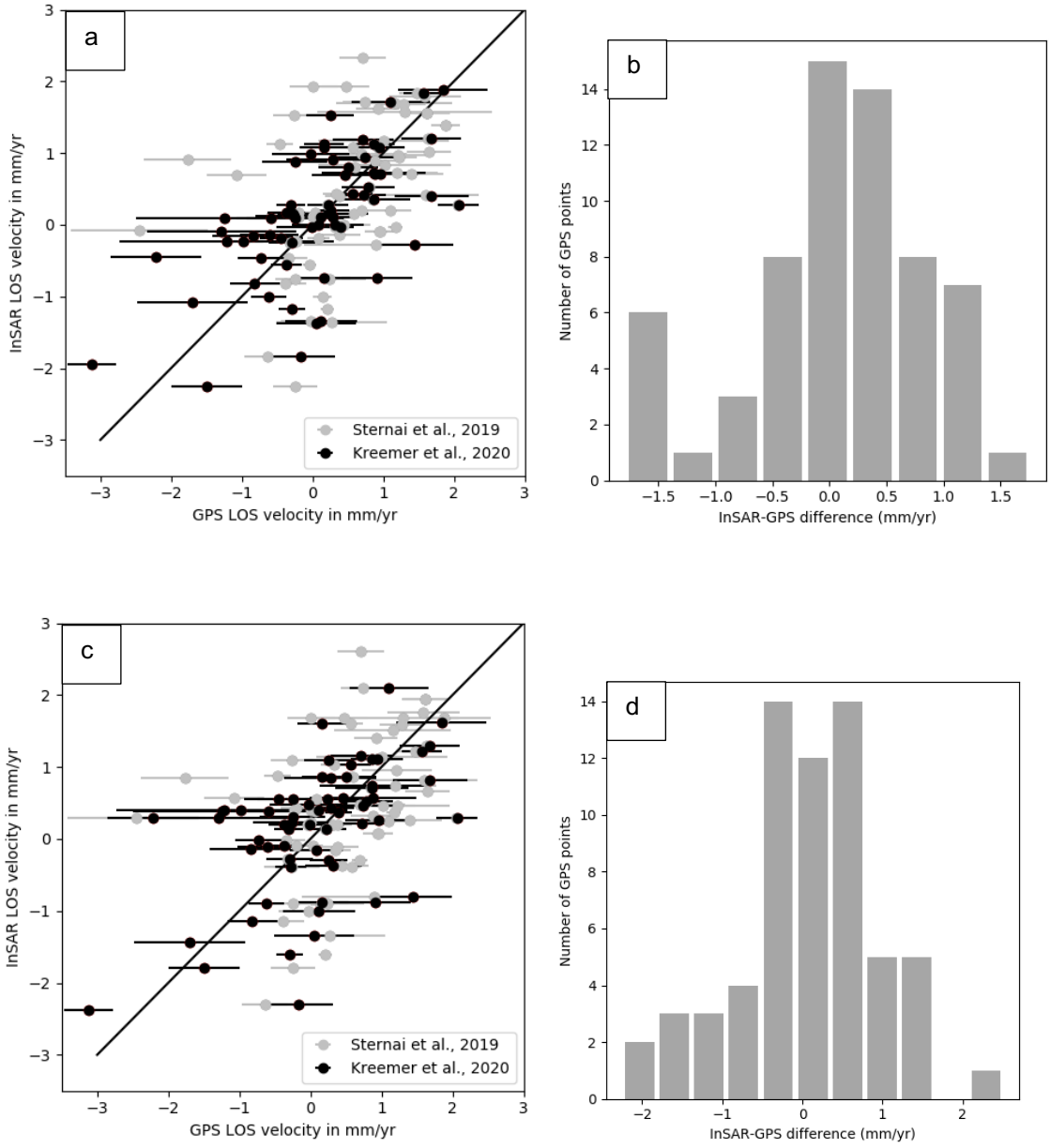

Figure S4. Comparison of InSAR and GPS LOS velocities, after spatial smoothing of InSAR velocity solutions and after adding a ramp in range and azimuth on InSAR data to adjust GPS data from Kreemer et al., 2020. Scatter plots of (a) APS-weighted and (c) median-filtered InSAR solutions versus GNSS solutions, along with y=x line. The correlation coefficient between APS-weighted/median-filtered and Kreemer et al. GPS data is 0.64/0.53 respectively. b) and d) show histograms of the 63 common LOS InSAR-GPS measurement differences, with a standard deviation of 0.79 mm/yr and 0.91 mm/yr, respectively.

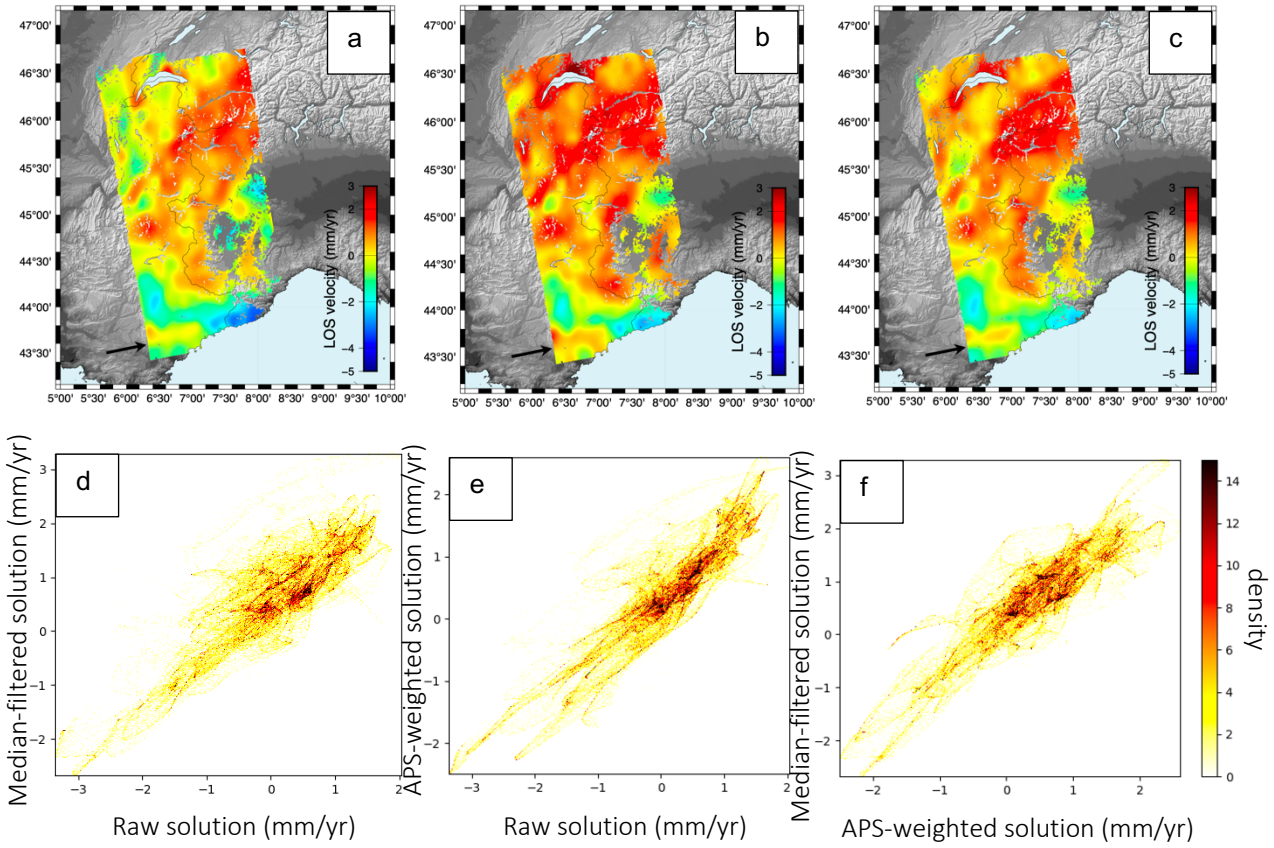

Figure S5. Quantitative comparison of the three velocity solutions obtained jointly with seasonal signal estimation (Fig S2 b), d), and f)), after referencing to the GNSS solution from Kreemer et al. (2020) and after spatial smoothing using a Gaussian kernel. a) "raw" solution (no weighting of outliers in the time series). b) "median-filtered" solution. c) "APS-weighted" solution. d), e), f) density scatter plots of velocity solutions plotted against each other.